

Deep-Learning-Based Catalog of Background Seismicity and Aftershocks of the 2020–2021 Large Earthquakes Along the Alaska Peninsula

Yaqi Jie^{*1,2}, Songqiao Shawn Wei^{1,2}, Weiqiang Zhu³, Jeffrey Freymueller¹, and Julie Elliott¹

Abstract

The Alaska Peninsula section of the Alaska-Aleutian subduction zone shows significant along-strike variations in seismic activity and interseismic plate coupling. This region experienced the 2020 M_w 7.8 Simeonof megathrust, M_w 7.6 Sand Point strike-slip, and 2021 M_w 8.2 Chignik megathrust earthquakes. This study, utilizing deep learning techniques, presents a high-precision earthquake catalog, providing insights into background seismicity, aftershocks, and slab geometry. An abrupt change in the slab dip angle at 30–40 km depths in the Shumagin segment acted as a barrier to the Simeonof and Sand Point earthquake ruptures. The Simeonof event triggered more aftershocks in the overriding plate than the Chignik event, suggesting the overriding plate is more deformed and hydrated in the Shumagin segment. The Sand Point earthquake triggered numerous aftershocks in the overriding plate, delineating a fault in the overriding plate with similar geometry as the intraslab mainshock fault, but activated around seven days after the mainshock.

Cite this article as Jie, Y., S. S. Wei, W. Zhu, J. Freymueller, and J. Elliott (2025). Deep-Learning-Based Catalog of Background Seismicity and Aftershocks of the 2020–2021 Large Earthquakes Along the Alaska Peninsula, *Seismol. Res. Lett.* **XX**, 1–17, doi: [10.1785/0220250072](https://doi.org/10.1785/0220250072).

Supplemental Material

Introduction

The Alaska-Aleutian subduction zone is the most tectonically and seismically active convergent margin in North America. The Alaska Peninsula section of this subduction zone, with its diverse seismicity patterns, has been identified by the scientific community as a top site to address fundamental questions of subduction processes. This region, comprising several distinct segments identified through slip deficit distribution and seismic imaging, exhibits notable along-strike variations in both interseismic plate coupling and seismicity (Fig. 1). In particular, the “Shumagin seismic gap” first identified by Davies *et al.* (1981) remained unruptured by any $M > 8$ earthquakes for at least 200 yr, whereas the megathrust was ruptured by an M_w 8.3 earthquake in 1938 (Freymueller *et al.*, 2021) to the northeast and an M_w 8.6 earthquake in 1946 to the southwest (Davies *et al.*, 1981). In the fore-arc region between Kodiak Island and Shumagin Islands, the slip deficit decreases from northeast to southwest (Drooff and Freymueller, 2021; Xiao *et al.*, 2021), and slab dehydration and overriding plate hydration also become more extensive and intensive to the southwest (Wang *et al.*, 2025). These variations reflect the heterogeneous nature of the megathrust, likely influenced by sedimentary and crustal structures of the subducting slab, such as pre-existing fault systems (Shillington *et al.*, 2015), sediment layer thickness (Wei *et al.*, 2021), and the rigidity of the overriding plate (Shillington *et al.*, 2022).

Since 2020, a new megathrust sequence, including the 2020 M_w 7.8 Simeonof earthquake and the 2021 M_w 8.2 Chignik earthquake occurred offshore the Alaska Peninsula. Several coseismic slip models indicate that the 2020 Simeonof event ruptured the eastern part of the Shumagin gap at 25–45 km depths (Crowell and Melgar, 2020; Xiao *et al.*, 2021; Ye *et al.*, 2021). The slip occurred in localized patches, likely related to the rheological heterogeneity revealed by active-source P -wave tomography (Shillington *et al.*, 2022). Subsequently, the 2021 Chignik earthquake, located northeast of the 2020 Simeonof event and potentially triggered by it, ruptured the megathrust at 25–45 km depths and farther east into the 1938 M_w 8.3 earthquake rupture area (Elliott *et al.*, 2022; Liu *et al.*, 2022; Ye *et al.*, 2022). Active-source studies have identified significant changes in the plate interface dip angle and width (Shillington *et al.*,

1. Department of Earth and Environmental Sciences, Michigan State University, East Lansing, Michigan, U.S.A., <https://orcid.org/0000-0003-3431-6583> (YJ); <https://orcid.org/0000-0002-6217-0545> (SSW); <https://orcid.org/0000-0003-0614-0306> (JF); <https://orcid.org/0000-0001-6996-5706> (JE); 2. Department of Computational Mathematics, Science and Engineering, Michigan State University, East Lansing, Michigan, U.S.A.; 3. Department of Earth and Planetary Science, University of California, Berkeley, California, U.S.A., <https://orcid.org/0000-0003-2889-1493> (WZ)

*Corresponding author: jieyaqi@msu.edu

© Seismological Society of America

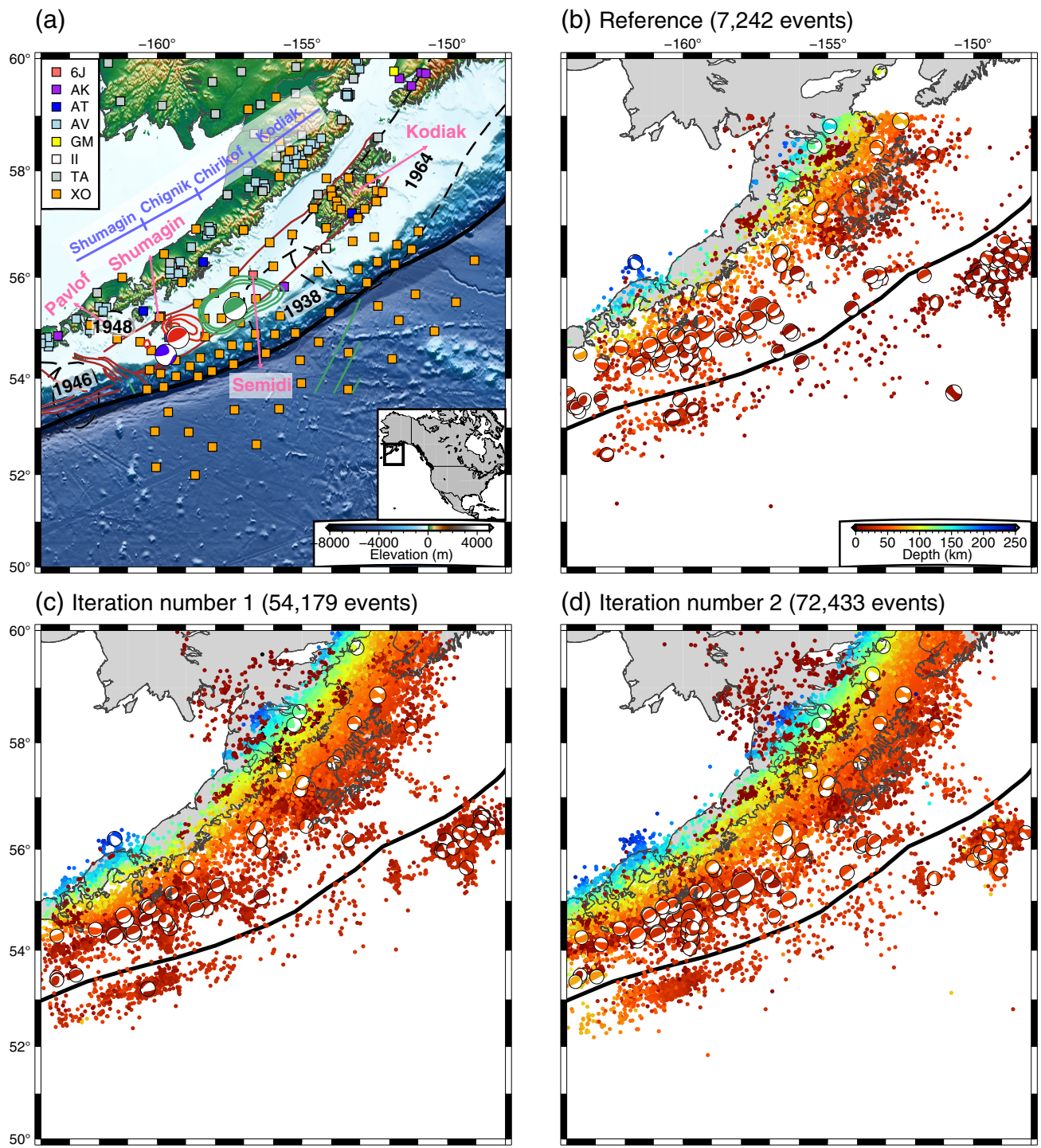


Figure 1. Maps of seismic stations and events. (a) Bathymetry and topography of the Alaska Peninsula and adjacent region. The squares represent seismic stations of various networks. The red, blue, and green focal mechanism plots indicate the 2020 M_w 7.8 Simeonof, 2020 M_w 7.6 Sand Point, and 2021 M_w 8.2 Chignik earthquakes, respectively. The coseismic slip models for the 2020 Simeonof and 2021 Chignik earthquakes are shown with 1, 1.5, and 2 m contours in red and green, respectively (Xiao et al., 2021; Elliott et al., 2022). The solid brown curves outline terrane boundaries and known faults in this region (Horowitz et al., 1989). The black dashed contours outline the rupture zones of previous megathrust earthquakes (Davies et al., 1981) and the 1 m contour of the 1938 M_w 8.3 earthquake slip model (Freymueller et al.,

2021). The light blue bars illustrate the four segments discussed in this article, following Wang et al. (2024), and the pink arrows denote the islands mentioned in the text. The inset map shows the location of the study area. Gray shading denotes the North America Plate, and the black box outlines the study region. (b) The reference catalog from May 2018 to August 2019 manually examined by the Alaska Earthquake Center (AEC). Earthquakes are color-coded by depth with Global Centroid Moment Tensor (Global CMT) focal mechanisms shown as focal mechanism plots. The bold black line represents the trench, and the gray lines depict the coastline. (c) Iteration number 1 output catalog. (d) Iteration number 2 output as the final catalog. The color version of this figure is available only in the electronic edition.

2022), potentially providing rupture barriers to the Simeonof and Chignik earthquakes.

About three months after the Simeonof earthquake, an M_w 7.6 strike-slip event, called the Sand Point, occurred nearby. It originated inside the subducting slab with the fault plane nearly aligned with the slab dip. This event has been attributed to several causes, including stress changes produced by the Simeonof earthquake (Jiang *et al.*, 2022; Yang *et al.*, 2023; Senapati *et al.*, 2024), abrupt coupling changes (Herman and Furlong, 2021; Jiang *et al.*, 2022), and pre-existing structures from the incoming and overriding plate (Clarke *et al.*, 2024). This strike-slip event generated an unexpected tsunami with wave heights higher than those produced by the larger Simeonof megathrust event. Bai *et al.* (2023) proposed a three-fault coseismic model to fit the tsunami data, although after including more Global Positioning Sys data (Grapenthin *et al.*, unpublished manuscript, see Data and Resources) favored a single-fault model with additional contributions from slip on the plate interface.

In this study, we explore the three 2020–2021 earthquakes by building a high-precision regional earthquake catalog powered by deep learning techniques. Deep learning has demonstrated its ability to detect an order of magnitude more events than conventional catalogs examined by human analysts (Mousavi and Beroza, 2022). The resulting increase in detected earthquakes enables more detailed spatial and temporal analysis of aftershocks and helps delineate fault systems (Park *et al.*, 2020; Tan *et al.*, 2021). With more information about the background seismicity and aftershocks of these earthquakes, we provide new insights into the three mainshocks as well as subduction zone processes.

Data and Methods

Data and reference catalog

We used seismic data recorded by 218 stations from January 2018 to December 2022 (Fig. 1a). These stations include those from permanent networks (network codes: II, GM, AK, AT, and AV), as well as temporary stations from the EarthScope USArray (network code: TA), ocean-bottom seismographs (OBSs) and land-based seismic stations from the Alaska Amphibious Community Seismic Experiment (AACSE, network code: XO), and a 1-year temporary seismic array deployed immediately after the 2021 M_w 8.2 Chignik earthquake (network code: 6J). Only data from broadband stations were utilized.

We assembled a reference catalog of local earthquakes, consisting of 7,242 events, 212,853 P -wave arrivals, and 100,292 S -wave arrivals from May 2018 to August 2019, which were manually picked by the Alaska Earthquake Center (AEC) (Ruppert *et al.*, 2022; Fig. 1b). Based on this reference catalog, we created a reference dataset by selecting 5 min before and after each P -wave arrival, ensuring to include the corresponding S -wave arrival from the same event. Time windows containing only S phases without P phases were discarded to maintain data quality. Traces with missing data were filled with zeros, and

missing channels were also replaced with zero-filled traces. All three-component waveforms were detrended, demeaned, tapered, and resampled to 40 Hz. Because about half of the stations were operated with a sample rate of 100 Hz, this down-sampling approach potentially leads to the loss of high-frequency signals recorded by some stations. However, because all the training, validation, testing, and continuous data are consistently resampled to 40 Hz, this approach should not introduce systematic bias to phase picking.

We also assembled a continuous dataset from January 2018 to December 2022 by cutting waveforms into 10-day segments and processing them in the same manner as the reference dataset. Given the large data volume, exceeding 2 TB in miniSEED format, the dataset construction was facilitated by the mseedindex package and ObsPy wrapper (Beyreuther *et al.*, 2010) to ensure efficient data access and improved input/output performance.

Earthquake detection and relocation

To develop a new earthquake catalog, we use a semi-supervised learning workflow (Xi *et al.*, 2024) starting with PhaseNet-TF to pick phases, then associating phases with GaMMA-1D, and finally relocating earthquakes with tomoDD. This process is iterated twice. We use the reference dataset for training in iteration number 1, and use the output of iteration number 1 for training in iteration number 2. Previous experience (Xi *et al.*, 2024) shows that two iterations are sufficient to obtain a nearly complete catalog.

PhaseNet-TF was initially trained and applied to a dataset in the Tonga subduction zone (Xi *et al.*, 2024) and showed a much better performance in picking S waves at OBSs and land stations compared to its predecessor PhaseNet (Zhu and Beroza, 2019). Because the tectonic setting, instrument types, and earthquake mechanisms at the Alaska Peninsula differ from those in Tonga, we retrain the PhaseNet-TF model using the reference dataset to optimize performance. The PhaseNet-TF Alaska model is trained for a maximum of 400 epochs with potential early stopping to prevent overfitting, achieving an F1 score higher than 0.97 on the test dataset. We then apply this model to the continuous dataset to obtain probabilities for P - and S -wave arrivals. Peak probabilities higher than 0.5 are considered positive picks, resulting in more than 9,000,000 picks. In iteration number 1, training and predicting took 37 and 163 hr on eight graphic processing units (GPUs), respectively. In iteration number 2, with a 6 times larger training dataset, training and predicting took 185 hr on 16 GPUs and 163 hr on 8 GPUs, respectively.

Next, we associate PhaseNet-TF output picks using GaMMA-1D, a Bayesian Gaussian Mixture Model Associator with a 1D velocity structure. Compared to its predecessor GaMMA (Zhu *et al.*, 2022), this new version utilizes a 1D velocity model, which is necessary for associating arrivals of events deeper than 30 km. In this study, the velocity model comes from averaging previous 3D shallow (0–240 km; Wang *et al.*, 2024)

and deep (240–400 km; [Wang et al., 2025](#)) tomography models in this region. Events with fewer than ten picks are discarded before further relocation. Associating more than 9,000,000 picks took only 2 hr on 20 central processing units, resulting in a preliminary catalog of over 150,000 events. After the initial association, we then refine the earthquake locations using a resampling strategy adapted from the Random Sample Consensus algorithm ([Zhu et al., 2025](#)). For each event, we locate it with random subsets of the associated picks to identify and exclude outlier picks. Because of the large uncertainties associated with estimating magnitudes of small earthquakes, we excluded the magnitude information from the new catalog to avoid additional uncertainties.

We use tomoDD ([Zhang and Thurber, 2003](#)), a double-difference tomography and relocation package, to relocate earthquakes. We fix the 3D velocity structure as the combined model from [Wang et al. \(2024\)](#) and [Wang et al. \(2025\)](#) and only invert for the locations and origin times of earthquakes. We estimate uncertainties with a bootstrap resampling strategy. We create 100 datasets, each consisting of 80% random P- and S-wave arrivals for relocation. The output catalog is relocated using the complete dataset, whereas the uncertainties of location and origin time of each event are computed from the standard deviations of the 100 bootstrap resampling inversions. We discard events with uncertainties exceeding 0.05° in longitude, 0.1° in latitude, 5 km in depth, or 1 s in origin time for future discussion. In addition, we also discard events with station azimuthal gaps greater than 270°, many of which are offshore events before or after the AACSE deployment.

After iteration number 1, the output catalog contains 110,147 events, of which 32,036 events fall within the same time range as the reference catalog (May 2018 to August 2019). 54,177 events, along with 1,253,058 P- and 528,190 S-wave arrivals, are retained to construct the training dataset for iteration number 2 (Fig. 1c). Because of our high-quality control requirements, 31,316 P- and 17,231 S-wave manually picked arrivals in the reference catalog are not included in the iteration number 1 output catalog. By combining these arrivals, we have a new dataset consisting of 59,968 events, 1,284,374 P-, and 545,421 S-wave arrivals with a size of 692 GB, 6 times larger than the reference dataset. We then use this dataset to retrain PhaseNet-TF and conduct a second iteration of phase picking, phase association, and event relocation to produce the final catalog (Fig. 1d). In addition, we associate the final catalog with the Global Centroid Moment Tensor (Global CMT) catalog ([Dziewonski et al., 1981](#); [Ekström et al., 2012](#)) to obtain the moment magnitude and focal mechanism parameters of large events.

Results

Final catalog and assessments

The final catalog, output of iteration number 2, contains 117,151 events with 2,631,256 P- and 1,091,693 S-wave arrivals in

2018–2022, about 30 times larger than the International Seismological Center (ISC) Reviewed Bulletin ([Bondár and Storchak, 2011](#); [International Seismological Center \[ISC\] Bulletin, 2018](#)) during the same period. In addition, our catalog contains about 5 times more events than the AEC catalog ([Ruppert et al., 2022](#)) during the overlap time from May 2018 to August 2019. 72,434 of these events have a spatial uncertainty (square root of the sum of the squares of horizontal and vertical uncertainties) lower than 5 km (Fig. 1d) and are used for the following discussions. Figure 2 shows examples of spectrograms, waveforms, and prediction probabilities for both shallow (< 50 km) and deep earthquakes (> 50 km) at one land station and one OBS, highlighting the robustness of the PhaseNet-TF Alaska model in accurately identifying phase arrivals.

We evaluate the earthquake detection/relocation performance against the AEC-picked reference catalog from May 2018 to August 2019 (Table 1). The recall, precision, and F1 metrics are calculated based on the numbers of true positives, false positives, and false negatives. An arrival with a time difference of 3 s or less compared to the reference is considered a true positive, whereas an event is treated as a true positive if it has a majority of matching phases and its origin time is within 15 s compared to the reference. Iteration number 1 achieves recall rates of 0.93 for P-wave arrivals, 0.94 for S-wave arrivals, and 0.95 for events. After iteration number 2, the final catalog successfully autodetects 95% of the earthquakes from the AEC-picked reference catalog. 5% of the events are missed because each of them has less than 10 phases or has large relocation uncertainty, and we do not use all AEC stations out of the Alaska Peninsula. More metrics are listed in Table 1.

Although many offshore earthquakes in our catalog lack offshore constraints, we are still confident in most of their depths. From a methodological perspective, the double-difference relocation algorithm integrates the 5-year onshore data with the 15-month AACSE offshore data into the same inversion, so that the OBS data can help constrain the earthquakes that occurred before or after the AACSE deployment. More importantly, the relocated hypocenters of the Simeonof and Chignik mainshocks and most aftershocks (see the [Aftershocks in the overriding plate](#) section) coincide with the plate interface independently determined by active-source seismic studies ([Kuehn et al., 2024](#)). This coincidence provides strong independent evidence for the reliability of the majority of our relocated earthquake depths and locations. About 10 events located deeper than 50 km beneath the fore-arc seem tectonically impossible. Careful manual examinations suggest that these events are false detections. Because our methods are based on statistics and these events constitute only 0.01% of the entire catalog, we avoid using a subjective way to discard them.

Comparing different deep learning methods

We first assess the associator by applying different versions of GaMMA to the AEC manually labeled phase arrivals (Fig. 3,

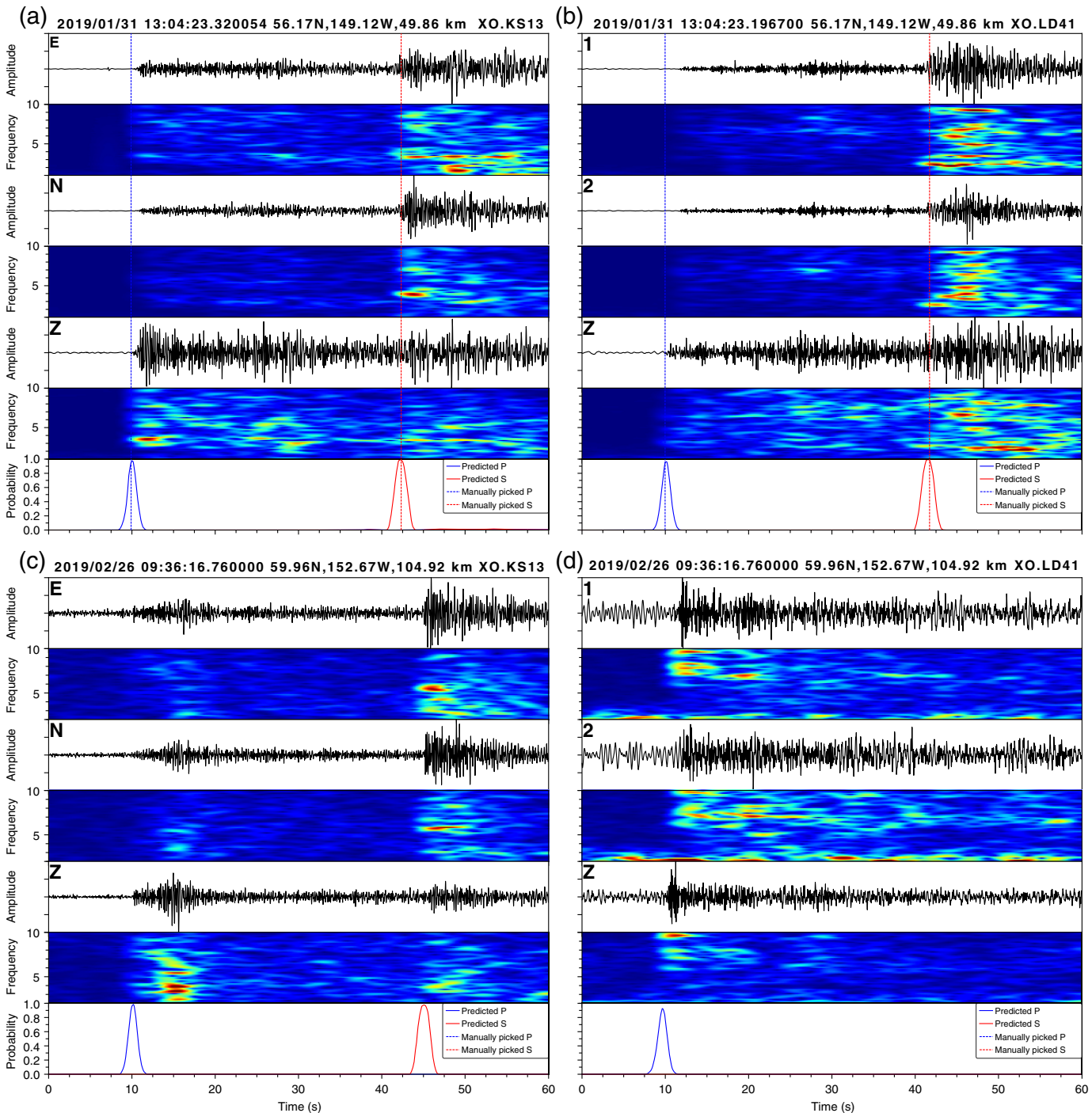


Table 2). When using GaMMA-1D, the performance of both association and relocation improves significantly, as seismic velocity changes dramatically with respect to depth in a subduction zone. For instance, GaMMA incorrectly splits single earthquakes into multiple events in the outer-rise, resulting in numerous artificially deep earthquakes (Fig. 3c). GaMMA-1D addresses this issue by generating more accurate synthetic travel-time estimates using a 1D velocity model, which enhances the reliability of phase association and improves the precision of earthquake locations. Using a 3D velocity model

Figure 2. Examples of PhaseNet-TF picking on continuous data. Each panel displays the event origin time, event latitude, longitude, depth, and network station in the title. (a) A shallow event (<50 km) recorded by a land station. (b) The same shallow event recorded by an ocean-bottom seismometer (OBS). (c) A deeper event (>50 km) recorded by a land station. (d) The same deeper event recorded by an OBS. The color version of this figure is available only in the electronic edition.

TABLE 1
Assessment for Prediction, Association, and Relocation in Iteration Number 2

Stage	Phases	Autodetected	Manual Pick	True Positive	False Positive	False Negative	Precision	Recall
Phase picking	<i>P</i> phase	4,815,991	212,853	207,207	4,608,784	5,646	0.04	0.97
	<i>S</i> phase	952,109	100,292	99,585	852,524	707	0.10	0.99
Association	<i>P</i> phase	1,135,419	212,853	198,817	936,602	14,036	0.18	0.93
	<i>S</i> phase	435,284	100,292	82,361	352,923	17,931	0.19	0.82
	Event	43,719	7242	7,153	36,566	89	0.16	0.99
Relocation	<i>P</i> phase	971,284	212,853	191,939	779,345	20,914	0.20	0.90
	<i>S</i> phase	399,031	100,292	80,427	318,604	19,865	0.20	0.80
	Event	34,834	7,242	6,845	27,989	397	0.20	0.95

Performance is evaluated against the Alaska Earthquake Center (AEC)-picked reference catalog from May 2018 to August 2019.

potentially improves the association performance but will significantly increase the computational demand, which is unnecessary at this stage. The use of an Alaska-specific velocity model further enhances the association performance, particularly for deep events. These improvements ensure robust association and relocation, providing a solid foundation for comparing the phase-picking models. All the following tests in this section use GaMMA-1D with a 1D Alaska velocity model and the same relocation processes.

To further evaluate phase pickers, we compare our PhaseNet-TF Alaska model with two other deep learning models: PhaseNet-TF Tonga trained with land-station and OBS data in the Tonga subduction zone ([Xi et al., 2024](#)) and Earthquake Transformer (EQT) trained with global data ([Mousavi et al., 2020](#)). This comparison is conducted on two months of continuous data from January to February 2019, during the operation period of most OBSs and land stations (Fig. 4, Table 3).

The new PhaseNet-TF Alaska model significantly improves the performance, not only detecting more events, but also achieving a recall of 0.98, much higher than the EQT global model's recall of 0.81 and the PhaseNet-TF Tonga model's recall of 0.67 (Fig. 4, Table 3), even though the PhaseNet-TF Tonga and EQT models pick more arrivals. The comparison between the PhaseNet-TF Alaska (Fig. 4b) and PhaseNet-TF Tonga (Fig. 4d) models highlights the importance of training with local data. Although the Tonga model is trained with data after removing instrumental responses, the performance difference is minimal when applied to data with or without instrumental response (recall of 0.98 versus 0.98, Table 3). Thus, removing the instrumental response does not significantly impact the performance, saving computational resources in future catalog building.

Neither the EQT nor the PhaseNet-TF Tonga model is trained with local data, but the latter obviously outperforms the former (Fig. 4c,d). Although EQT's deep encoder and attention layers may reduce phase arrival uncertainty ([Mousavi et al.,](#)

[2020](#)), our results show that it is unsuitable for the Alaska dataset with both OBS and land stations and thus generates numerous false picks and events. PhaseNet-TF performs better due to incorporating spectrograms in the time-frequency domain.

Discussion

Slab dip angle change affects megathrust rupture

The new catalog shows the background seismicity before June 2020 and abundant aftershocks of the 2020 M_w 7.8 Simeonof and 2021 M_w 8.2 Chignik earthquakes (Fig. 5). We use the background seismicity (black dots in Fig. 5) to determine the plate interface below 40 km, as all intermediate-depth earthquakes occur in the slab crust and mantle. We also estimated the dip angle uncertainty by considering the spatial uncertainty of the relocated earthquakes. By combining this information with previous active-source seismic images of the top 40 km in this region ([Kuehn et al., 2024](#)), we build a new model of the plate interface geometry shown as red dashed curves in Figure 5. In addition, we define the aftershocks of these three major events following [Tape and Lomax \(2022\)](#). The relationship between coseismic rupture and aftershock distribution has been discussed in many previous studies and still remains controversial. Traditionally, aftershock distributions are used to outline mainshock rupture areas (e.g., [Davies et al., 1981](#); [Tape and Lomax, 2022](#)). On the other hand, [Wetzler et al. \(2018\)](#) suggest that regions of high coseismic slip often exhibit fewer aftershocks, resulting in a generally complementary pattern between the two. In this study, the aftershocks within 30 days after the mainshocks, combined with the coseismic slip models by [Elliott et al. \(2022\)](#) and [Xiao et al. \(2021\)](#), shed light on the coseismic and postseismic deformation of the three major events. We also compared the aftershocks with the coseismic slip models from [Ye et al. \(2021, 2022\)](#) in Figure S1, available in the supplemental material to this article, leading to the same interpretations.

The new plate interface model shows a rapid change in the slab dip angle at 30–40 km depths in the Shumagin segment

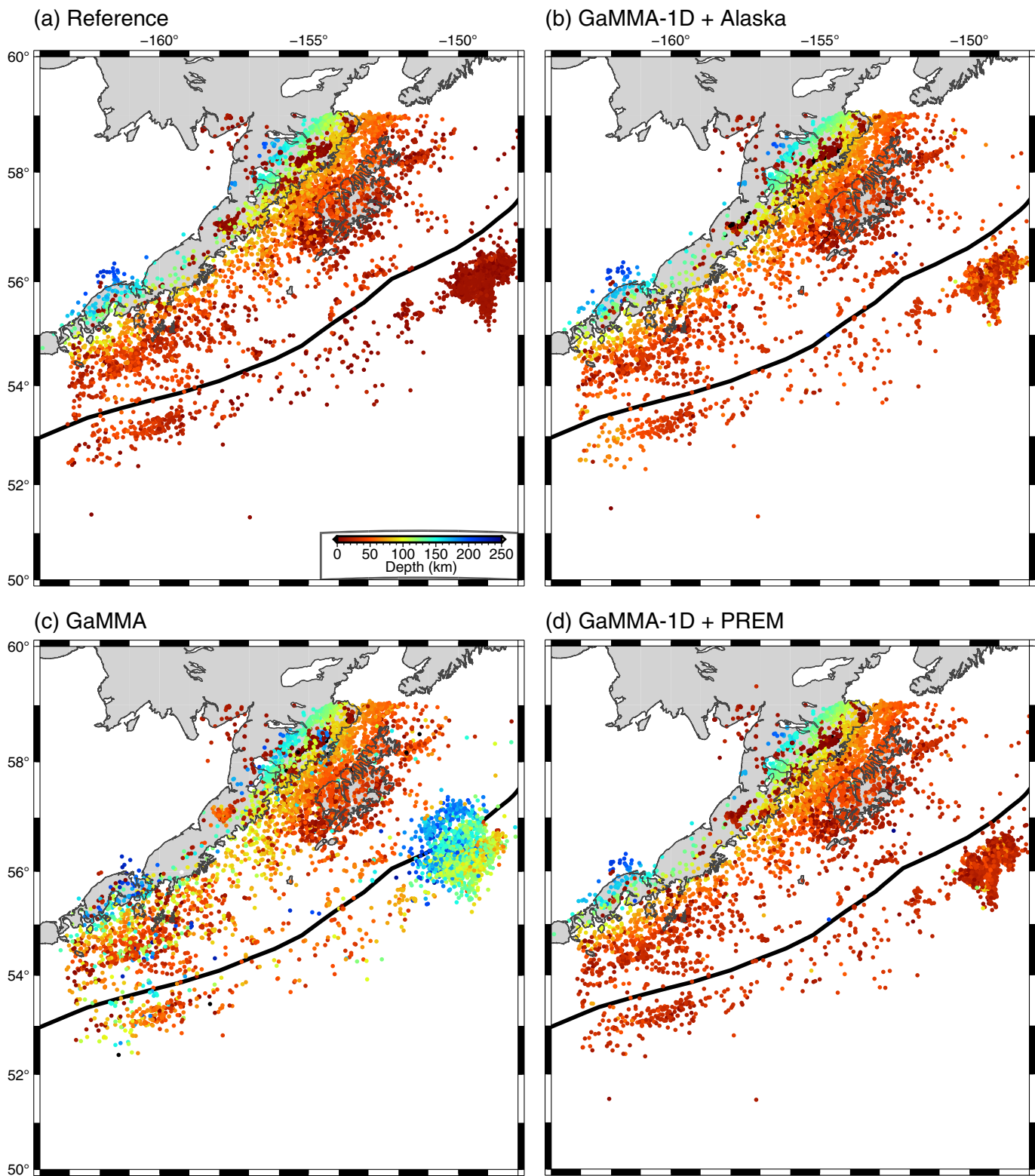


Figure 3. Catalogs from manual pick tests. All the catalogs are generated using AEC manually labeled phase arrivals, applying different associators but following the same relocation process. All other features are the same as Figure 1b. (a) The reference catalog from May 2018 to August 2019 was manually examined

by the Alaska Earthquake Center (AEC). (b) Catalog associated using GaMMA-1D with the Alaska velocity model. (c) Catalog associated using GaMMA. (d) Catalog associated using GaMMA-1D with the PREM velocity model. The color version of this figure is available only in the electronic edition.

TABLE 2
Association and Relocation Result for Alaska Earthquake Center (AEC) Manual Picks in Iteration Number 2

Method	Phase	Relocated	Reference Catalog	True Positive	False Positive	False Negative	Precision	Recall	F1
GaMMA	<i>P</i> phase	139,863	212,850	137,451	2,412	75,399	0.98	0.65	0.78
	<i>S</i> phase	67,507	100,292	66,184	1323	34,108	0.98	0.66	0.79
	Event	6,944	7,242	6,767	177	475	0.97	0.93	0.95
GaMMA-1D with PREM model	<i>P</i> phase	201,512	212,850	201,294	218	11,556	1.00	0.95	0.97
	<i>S</i> phase	90,226	100,292	90,134	92	10,158	1.00	0.90	0.95
	Event	6,957	7,242	6,945	12	297	1.00	0.96	0.98
GaMMA-1D with Alaska model	<i>P</i> phase	202,503	212,850	202,281	222	10,569	1.00	0.95	0.97
	<i>S</i> phase	93,341	100,292	93,249	92	7,043	1.00	0.93	0.96
	Event	6,978	7,242	6,967	11	275	1.00	0.96	0.98

Performance is evaluated against the AEC-picked reference catalog from May 2018 to August 2019. PREM, preliminary reference Earth model.

(Fig. 5 C–C' and D–D'), in which the dip angle increases from 13.4° above 30 km depth to $30.6 \pm 2.1^\circ$ at 40–100 km depths. Although Kuehn *et al.* (2024) do not estimate the slab dip uncertainty above 30 km depth, the lower bound of the slab dip angle below 40 km is significantly greater than the shallow dip angle. This dip angle change is most prominent in the western Shumagin segment, gradually fading away toward the east until it becomes indistinguishable in the Chignik segment. This feature is also observed in active-source seismic reflection images along ALEUT lines 4 and 5 (Shillington *et al.*, 2022; Fig. S2). Recent studies suggest that slab dip is controlled by subduction duration, with additional influence from the nature of the overriding plate and convergence rate, where thicker lithosphere with faster convergence tends to produce flatter dips (Hu and Gurnis, 2020). Given the similar subduction duration along the Alaska Peninsula and the existence of the Shumagin Islands, we suspect that the thicker continental crust of the Shumagin Islands than the surrounding fore-arc crust may be responsible for the slab dip angle change.

This slab dip angle change at 30–40 km depths coincides with changes in the aftershock distribution and coseismic deformation of the 2020 M_w 7.8 Simeonof earthquake. Coseismic modeling indicates that the mainshock ruptured the megathrust at 20–45 km depth, with the most slip concentrating in a narrow zone at 25–40 km depth, propagating primarily to the west from the hypocenter (Crowell and Melgar, 2020; Xiao *et al.*, 2021; Ye *et al.*, 2021). Most megathrust aftershocks were confined in the Shumagin segment, extending westward and landward from the mainshock hypocenter and coseismic peak slip area. On the western end of the rupture area, most aftershocks concentrated at 30–40 km depths along the plate interface (Fig. 5 C–C'), whereas on the eastern side, aftershocks extended up-dip to about 25 km depth (Fig. 5 E–E'). Therefore, our results, along with coseismic slip models, show that the coseismic and

postseismic deformation of the western portion of the 2020 M_w 7.8 Simeonof rupture area was mainly confined at 30–40 km depths on the megathrust, where the slab dip angle changes rapidly. In contrast, the 2021 M_w 8.2 Chignik earthquake ruptured a wider portion of the megathrust along-dip at 20–45 km depths without an obvious change in the slab dip angle. Similarly, the aftershock distribution is wider than that of the 2020 event, ranging from 20 to 45 km depth, although most aftershocks are up-dip. In sum, both coseismic slip models and aftershock distributions suggest that the western portion of the 2020 M_w 7.8 Simeonof earthquake ruptured the megathrust in a relatively narrow zone along the dip (30–40 km depths), whereas the 2021 M_w 8.2 Chignik event rupture area was much wider.

The contrast between the Simeonof and Chignik rupture areas suggests that the slab dip angle change may play a role in controlling rupture propagation. Fault geometry significantly influences seismicity and slip distribution (Segall and Pollard, 1980; Ben-Zion and Rice, 1995) because bends and segmentations often act as barriers to rupture propagation (Aki, 1979). Various global earthquakes support this phenomenon; for example, the 2007 M_w 7.7 Tocopilla earthquake rupture was likely inhibited by an abrupt dip angle change (Contreras-Reyes *et al.*, 2012), and a lateral change in the dip angle limited the rupture propagation of the 2015 M_w 7.8 Gorkha earthquake (Zhang *et al.*, 2017). Along the Alaska Peninsula in the Shumagin segment, the abrupt slab dip angle change at 30–40 km depths likely inhibited the seaward propagation of the Simeonof earthquake rupture and triggered stress release in the overriding plate (see the *Aftershocks in the overriding plate* section). In contrast, the megathrust to the east, where the dip angle change was less pronounced, experienced less restriction and allowed for slightly shallower rupture during the Chignik earthquake. Other factors, such as plate interface roughness, slab hydration, and variations in the overriding

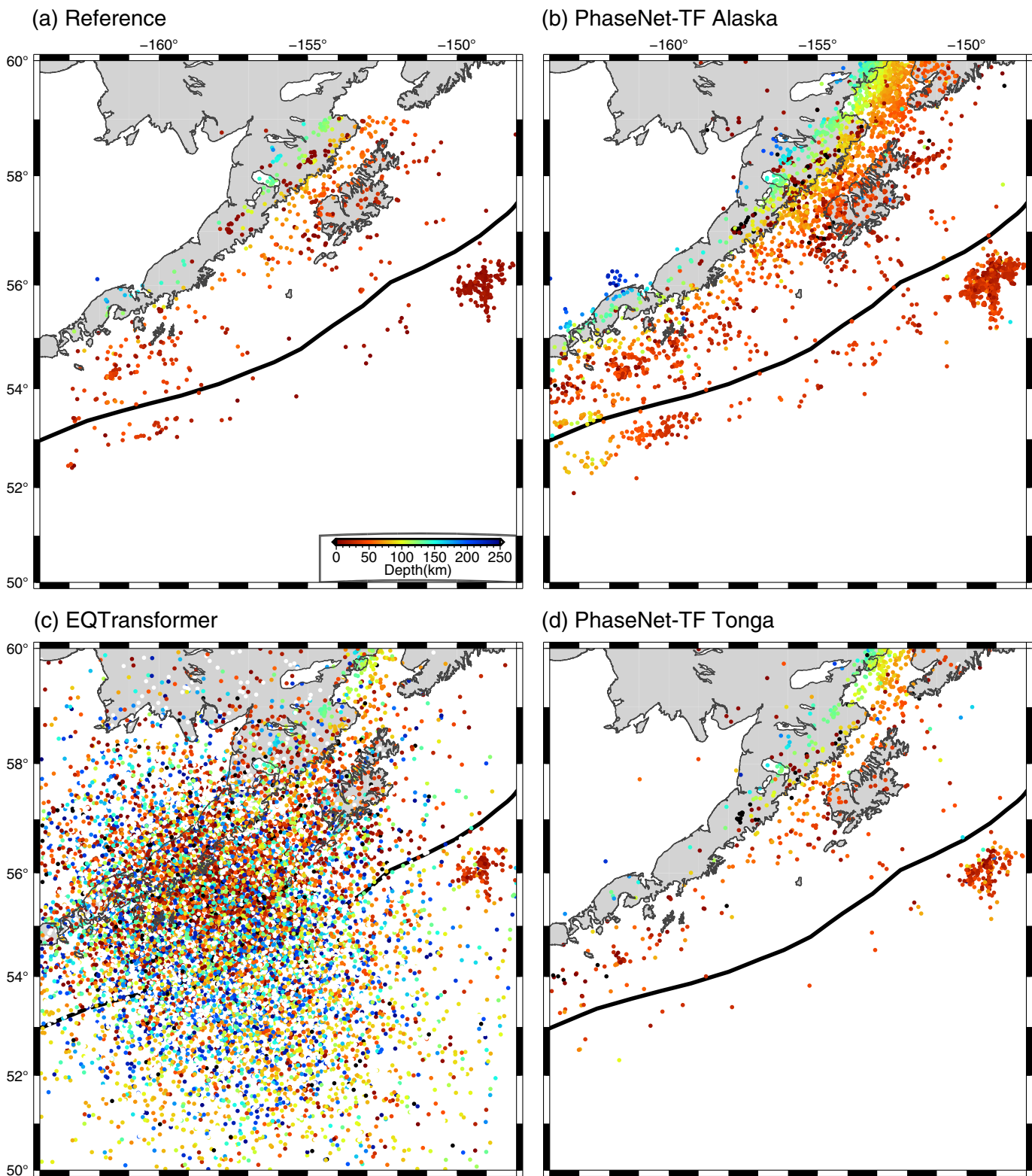


Figure 4. Catalogs comparing different deep learning models. All the catalogs are generated using phase arrivals picked by different models on data from January to February 2019, applying GaMMA-1D with the Alaska velocity model and the same relocation process. All other features are the same as Figure 1b. (a) The reference catalog from January to February 2019 was manually examined by the Alaska Earthquake Center (AEC).

(b) Catalogs generated from phase arrivals picked by PhaseNet-TF trained with the Alaska dataset. (c) Catalogs generated from phase arrivals picked by EQTransformer trained with the global dataset. (d) Catalogs generated from phase arrivals picked by PhaseNet-TF trained with the Tonga dataset. The color version of this figure is available only in the electronic edition.

TABLE 3
Comparison Between Different Deep Learning Phase Pickers on Two Months of Continuous Data from January to February 2019

Model	Phases	Autodetected	Manual Pick	True Positive	False Positive	False Negative	Precision	Recall
PhaseNet-TF Alaska	<i>P</i> phase	128,825	25,028	23,991	104,834	1,037	0.19	0.96
	<i>S</i> phase	54,752	11,754	10,922	43,830	832	0.20	0.93
	Events	4,467	740	728	3,739	12	0.16	0.98
PhaseNet-TF Alaska (Instrument response removed)	<i>P</i> phase	118,288	25,028	22,977	95,311	2,051	0.19	0.92
	<i>S</i> phase	52,801	11,754	10,164	42,637	1,590	0.19	0.86
	Events	4,251	740	728	3,523	12	0.17	0.98
PhaseNet-TF Tonga	<i>P</i> phase	21,036	24,965	10,523	10,513	14,442	0.50	0.42
	<i>S</i> phase	15,684	11,754	4,619	11,065	7,135	0.29	0.39
	Events	929	740	499	430	241	0.54	0.67
EQT Global	<i>P</i> phase	219,440	25,028	10,891	208,549	14,137	0.05	0.44
	<i>S</i> phase	125,044	11,754	2,262	122,782	9,492	0.02	0.19
	Events	27,910	740	595	27,315	145	0.02	0.80

Performance is evaluated against the Alaska Earthquake Center (AEC)-picked reference catalog. EQT, Earthquake Transformer.

plate strength and thickness, likely also play important roles (e.g., Shillington *et al.*, 2022; Liu *et al.*, 2023). These combined factors limited the Simeonof rupture propagation.

Aftershocks in the overriding plate

In addition to along-strike variations in the plate interface, the distribution of aftershocks within the overriding plate also shows significant differences. Within 30 days following the 2020 M_w 7.8 Simeonof mainshock, our catalog shows at least four distinct aftershock clusters extending from the plate interface to the overriding plate (Fig. 5 C–C', D–D', and E–E'). These aftershocks suggest the Simeonof mainshock activated a complex fault system within the overriding plate in the Shumagin segment, consistent with active-source images (Shillington *et al.*, 2022). This type of dynamic triggering has been observed globally. For instance, the 2010 Maule megathrust earthquake (M_w 8.8) in Chile triggered seismic slip on a normal fault within the overriding plate (Hicks and Rietbrock, 2015). In contrast, after the 2021 M_w 8.2 Chignik mainshock, fewer aftershocks occurred in the overriding plate during the first 30 days (Fig. 5 F–F', G–G', and H–H', Fig. 6c,d).

The activation of the fault system in the overriding plate after the 2020 M_w 7.8 Simeonof earthquake indicates that the overriding plate in the Shumagin segment is weaker compared to that in the Chignik segment. Previous seismic tomography studies show extremely low-velocity and high- V_p/V_s anomalies in the overriding plate of the Shumagin segment, suggesting a high degree of deformation and hydration in this

region (Li *et al.*, 2024; Wang *et al.*, 2024). Therefore, we attribute the abundant aftershocks in the relatively weak overriding plate of the Shumagin segment to intensive and extensive deformation and hydration because the fluids from slab dehydration increase pore pressure, inducing microcracking, and triggering earthquakes.

At the megathrust depths, the fluids released from slab dehydration primarily originate from water stored in pore spaces and loosely bound water within sediments and the upper oceanic crust. This process is largely determined by plate hydration in the outer-rise region and the thickness of sediments (Faccenda, 2014). Because the subduction of the Zodiac sediment fan influences both the Shumagin and Chignik segments, the primary along-strike change in hydration arises from the outer-rise geology. Shillington *et al.* (2015) proposed that the existing fabrics on the incoming plate intersect the trench at a smaller angle (<30°) in the Shumagin segment than in the Semidi segment, thereby promoting the development of outer-rise faults. This hypothesis is supported by recent bathymetric mapping results, which show the Shumagin segment with more extensive and larger faults compared to the Chignik segment (Clarke *et al.*, 2024). In agreement with these observations, our catalog also shows a significant number of outer-rise events in the Shumagin segment, whereas only a few such events are observed in the Chignik segment.

In sum, the aftershock distributions of the 2020 and 2021 major earthquakes confirm that the slab dehydration and overriding plate hydration are more intensive and extensive in the

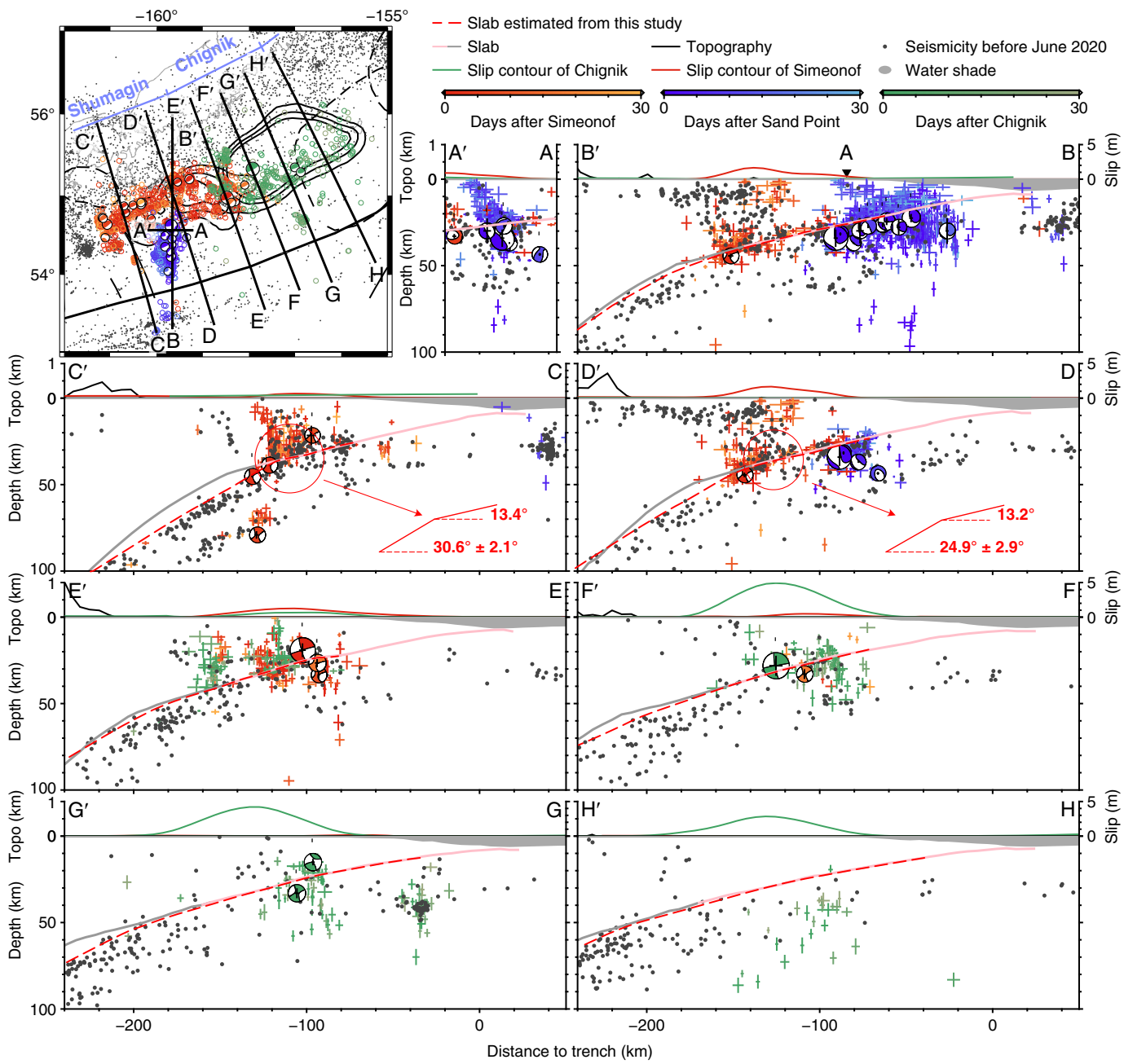


Figure 5. Map and cross sections of the final (iteration number 2) catalog. On the map, red, blue, and green circles represent aftershocks occurring within 30 days of the Simeonof, Sand Point, and Chignik mainshocks, respectively. The black dots indicate background seismicity before June 2020. On the map, straight lines indicate the cross sections shown in other panels, and other features are the same as in Figure 1b. The trench-normal cross sections have the same length from the trench, focusing on the main rupture areas at 20–50 km depths and 80–190 km from the trench. In each cross-section panel, crosses show the aftershocks of the three mainshocks with horizontal and vertical uncertainties (1-sigma). The black dots indicate the

background seismicity before June 2020. The black curve and gray area on the top represent topography and bathymetry, whereas the red and green curves show the coseismic slip distributions for the Simeonof (from Elliott et al., 2022) and Chignik (from Xiao et al., 2021) earthquakes, respectively. The pink and gray curves illustrate the slab surface (top of the plate interface) from Wang et al. (2024), based on a model constrained by active-source seismic experiments (pink, Kuehn et al., 2018) combined with the Slab2 model (gray, Hayes et al., 2018). The red, dashed curve indicates the revised plate interface based on the background seismicity relocation in this study. The color version of this figure is available only in the electronic edition.

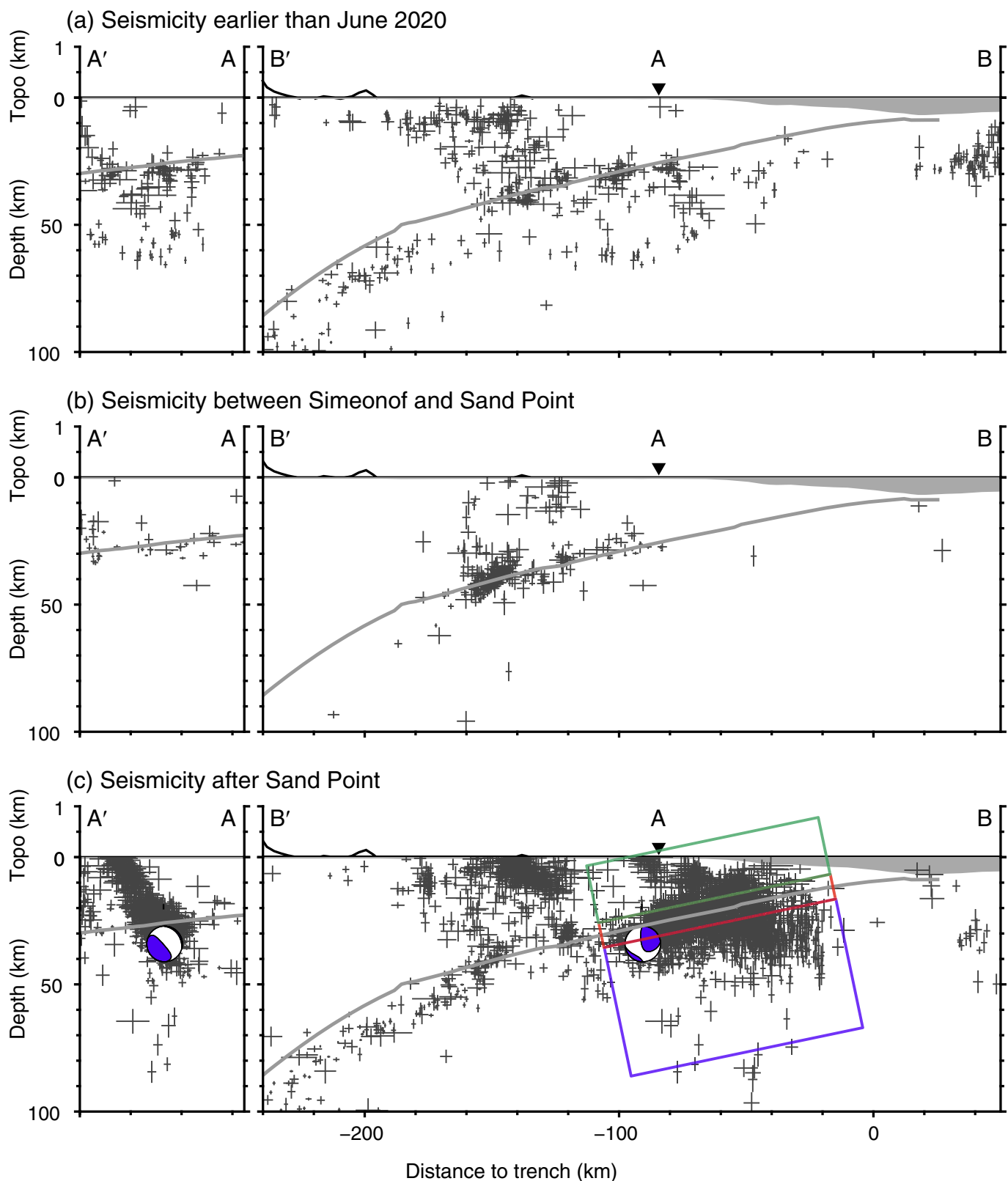
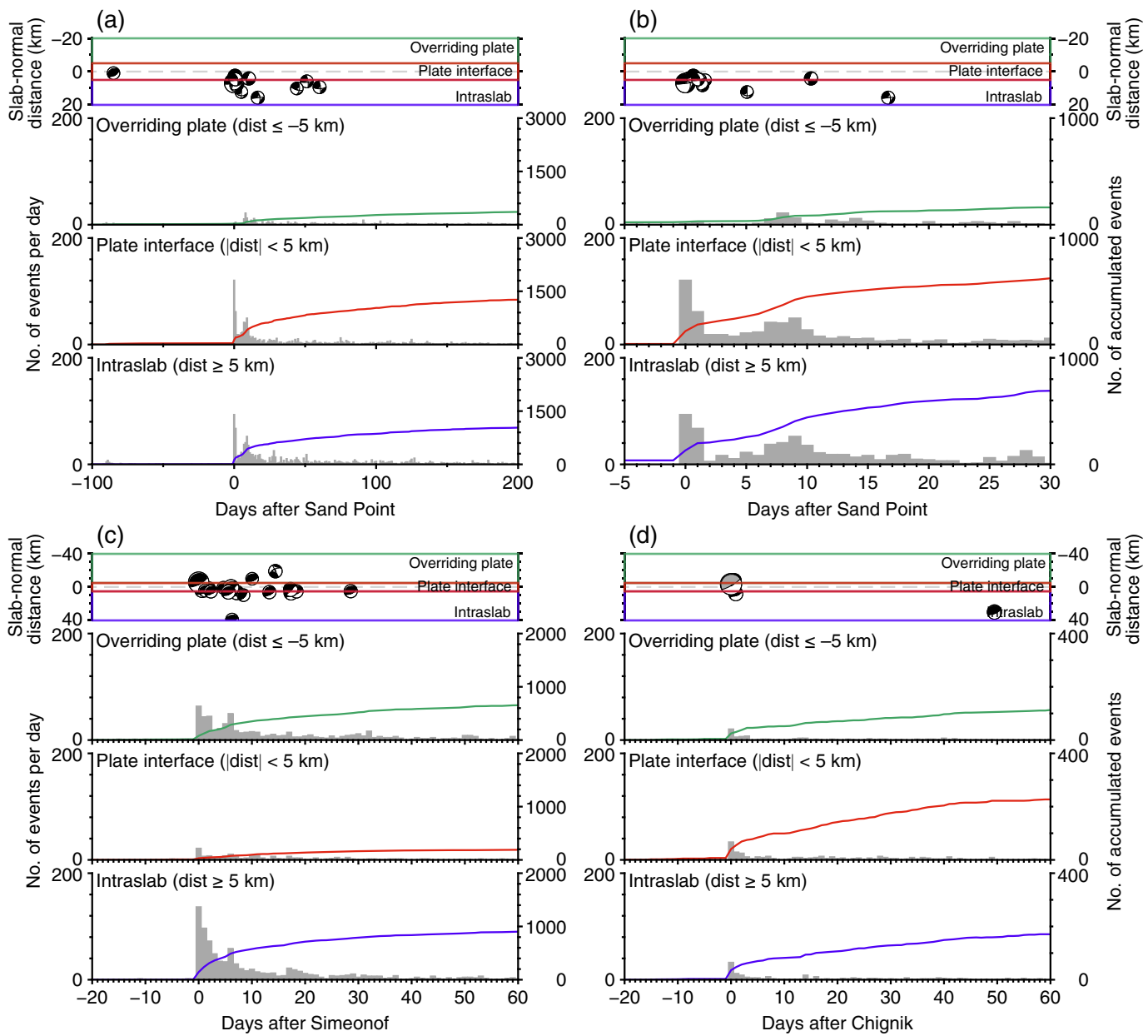


Figure 6. (a–c) Background seismicity and aftershocks of the 2020 Sand Point earthquake. The black crosses represent events with horizontal and vertical uncertainties. Other features are the same as in Figure 5. The green, red, and blue boxes in (c) denote the regions of the overriding plate, plate interface, and intraslab,

respectively, used for estimating temporal changes in Figure 7. Given the hypocenter uncertainties and plate interface thickness (Kuehn et al., 2024), we assume all events within 5 km above or below the slab surface occurred on the plate interface. The color version of this figure is available only in the electronic edition.



Shumagin segment than in the Chignik segment, as observed in previous tomography images (Shillington *et al.*, 2022; Li *et al.*, 2024; Wang *et al.*, 2024).

Complex fault system of the 2020 M_w 7.6 Sand Point strike-slip earthquake

The 2020 M_w 7.6 strike-slip event ruptured within the slab and unexpectedly generated a notable tsunami. Contrary to previous studies that mainly focus on the slab interior (Herman and Furlong, 2021), our catalog shows two clusters of aftershocks delineating two previously unmapped faults with almost identical strike and dip angles, one within the slab and the other in the overriding plate (Fig. 5 A–A' and B–B'). The intraslab fault is responsible for the mainshock, extending 10–15 km downward from the plate interface. Based on the distribution of the first-day aftershocks, the intraslab fault has a strike of 1°

Figure 7. Cumulative number of events and daily event rates before and after the three events. The top panels show events with Global CMT solutions plotted at their origin time and distance from the slab surface. Lower panels show event rates for the overriding plate, on the interface, and inside the subducting plate. (a) Number of events 100 days before and 200 days after the Sand Point earthquake. (b) Zoomed-in view of (a), showing 5 days before and 30 days after the Sand Point earthquake. (c) Number of events 20 days before and 60 days after the Simeonof earthquake. (d) Number of events 20 days and 60 days after the Chignik earthquake. The color version of this figure is available only in the electronic edition.

and a dip angle of 70°. The aftershocks in the overriding plate extended from the plate interface at ~25 km depth to the Earth's surface. If all of them occurred on a single fault, it would have a

strike of 5° and a dip angle of 52° on the first day of activation, and gradually change to a strike of 14°. Some of the aftershocks ruptured along the plate interface, with the lower bound coinciding with the slab dip angle change discussed in the [Slab dip angle change affects megathrust rupture](#) section, suggesting that the dip change also influenced the rupture propagation of the Sand Point intraslab earthquake.

Examining the background seismicity from January 2018 through June 2020 reveals few events along these faults. To further investigate the nature of these unmapped faults, we relocate all events with Global CMT solutions in the aftershock region back to 1970 with our catalog using the same setting and find that none align with the geometry of the two fault planes, indicating a long history of seismic quiescence. These faults are not identified in previous active-source studies or regional tectonic maps ([Bruns et al., 1987; Bécel et al., 2017; Shillington et al., 2022](#)) in which most identified faults dip northward. Based on Coulomb stress change studies ([Herman and Furlong, 2021; Elliott et al., 2022; Yang et al., 2023](#)), the Simeonof earthquake likely caused a maximum stress change of four bars in this region, insufficient to initiate a new fault plane in the overriding plate. Thus, we suspect that the aftershocks in the overriding plate delineate a pre-existing, unmapped fault system, possibly related to the backstop splay fault zone along the trench ([von Huene et al., 2021](#)).

To better understand the deformation in this region south of the Shumagin Islands, we plot the temporal evolution of seismicity before and after the M_w 7.8 Simeonof and M_w 7.6 Sand Point mainshocks (Fig. 6a–c). In addition, our high-precision catalog enables us to distinguish events in the slab from those in the overriding plate (Figs. 6c and 7b). The Simeonof earthquake on 22 July 2020 triggered overriding plate aftershocks near but more seaward of background seismicity and more plate-interface aftershocks down-dip to 40 km depth (Fig. 6a,b). After the Simeonof event, seismic activity did not increase significantly in the region where the Sand Point earthquake occurred. The Sand Point mainshock on 19 October 2020 triggered numerous aftershocks in a previously seismically quiet region closer to the trench (Fig. 6c). After the Sand Point mainshock, aftershock activity surged immediately in the slab and plate interface, with a second peak of activity seven days after the mainshock (Fig. 7b). This second peak coincides with the onset of aftershocks in the overriding plate. No big ($M > 5.5$) earthquake occurred on day 7 that could be potentially linked to this activation of faults in the slab, plate interface, and overriding plate.

Given the temporal and spatial distributions of aftershocks, we propose that the M_w 7.6 Sand Point ruptured within the slab and triggered slip along the megathrust. Shallow megathrust slip during or shortly after the main M_w 7.6 slip, possibly with a low amplitude, could generate a tsunami, as suggested by geodetic modeling and tsunamic simulation (Grapenthin *et al.*, unpublished manuscript, see [Data and Resources](#)).

Intriguingly, the overriding plate remained silent for 7 days after the mainshock before being ruptured by numerous aftershocks. We suspect this 7-day delay of overriding plate seismicity is related to fluid migration from the slab into the fore-arc crust, although we do not observe obvious aftershock migration in the overriding plate (Movie S1). We acknowledge that our catalog is probably incomplete, and some small aftershocks could have occurred within 7 days after the mainshock. However, given the same detection capability across the system, we are confident to conclude that the overriding plate was seismically inactive compared to the slab and plate interface immediately after the mainshock. Therefore, we suggest that the slip within the overriding plate was not responsible for generating the tsunami on 19 October 2020, in contrast to some studies that invoke overriding plate faults (e.g., [Bai et al., 2023](#)).

Conclusions

In this study, we examine complex seismic behaviors in the Alaska Peninsula region, focusing on the aftershocks of major earthquakes in 2020 and 2021. By integrating deep learning techniques, advanced phase picking, and improved association and relocation methods, we develop a high-precision earthquake catalog with 36 times more events than the ISC Reviewed Bulletin. Our findings suggest that slab geometry, particularly an abrupt dip angle change at 30–40 km depths in the Shumagin segment, may influence rupture propagation during both megathrust and intraslab events. The 2020 M_w 7.8 Simeonof earthquake rupture appears to have been inhibited from propagating up-dip by this dip change, likely inducing stress release in the overriding plate. In contrast, the 2021 M_w 8.2 Chignik earthquake ruptured a smoother megathrust, possibly facilitating more extensive up-dip rupture. Aftershocks in the overriding plate are more abundant and widespread in the Shumagin segment than in the nearby Chignik segment. We suggest that this contrast reveals a more deformed and hydrated overriding plate, likely resulting from more extensive and intensive slab dehydration in the Shumagin segment. The 2020 M_w 7.6 Sand Point aftershocks delineate two previously unmapped faults in the slab and overriding plate with nearly identical strikes and dip angles. The overriding plate fault was activated 7 days after the mainshock, but no big ($M > 5.5$) earthquakes could be linked to the onset of this fault activation.

Data and Resources

All data and codes associated with this study are publicly accessible and built on open-source platforms. PhaseNet-TF can be accessed at doi: [10.5281/zenodo.1487759](https://doi.org/10.5281/zenodo.1487759), and GaMMA-1D is available at doi: [10.5281/zenodo.1487760](https://doi.org/10.5281/zenodo.1487760). The compiled dataset is hosted on Hugging Face at doi: [10.57967/hf/4498](https://doi.org/10.57967/hf/4498), with model weights available at doi: [10.57967/hf/4499](https://doi.org/10.57967/hf/4499). The supplemental material includes cross sections of the final catalog with coseismic slip model from [Ye et al. \(2021, 2022; Fig. S1\)](#), cross sections of the final catalog along ALEUT Line 3, 4,

5 (Li *et al.*, 2015; Fig. S2), final earthquake catalog (Data Set S1), and a movie showing temporal evolution of seismicity before and after the 2020 M_w 7.6 Sand Point mainshock (Movie S1). Data processing and visualization were carried out using open-source packages, including ObsPy (<https://github.com/obspy/obspy/>) and GMT (<https://docs.generic-mapping-tools.org/latest/>). All seismic data used in this study were downloaded from EarthScope Consortium Web Services (<https://service.iris.edu/>) including the following seismic networks: (1) the II (Scripps Institution of Oceanography, 1986); (2) the GM (U.S. Geological Survey [USGS], 2016); (3) the AK (Alaska Earthquake Center, University of Alaska Fairbanks, 1987); (4) the AT (National Oceanic and Atmospheric Administration [NOAA], 1967); (5) the AV (Alaska Volcano Observatory/USGS, 1988); (6) the TA (Incorporated Research Institutions for Seismology [IRIS] Transportable Array, 2003); (7) the XO (Abers *et al.*, 2018); and (8) the 6J (Abers *et al.*, 2021). The unpublished manuscript by Grapenthin *et al.* (in revision), “Late triggered megathrust slip following the 2020 M_w 7.6 Sand Point Alaska strike-slip earthquake explains its tsunami,” submitted to *Seismica*.

Declaration of Competing Interests

The authors acknowledge that there are no conflicts of interest recorded.

Acknowledgments

The authors thank Yihe Huang and Demian Saffer for constructive discussions. This work was made possible by the support of National Science Foundation grants EAR-1942431 to S. S. W., EAR-2052558 and EAR-2152253 to S. S. W., J. T. F., and J. E. National Science Foundation Grant EAR-2147422 to J. T. F. and J. E. supported the rapid earthquake response to the Chignik earthquake, resulting in network 6J. The computing resources were made available through the ACCESS (Advanced Cyberinfrastructure Coordination Ecosystem: Services and Support) Grant EES240096, utilizing the Delta graphic processing units (GPU) system at the University of Illinois. The facilities of the EarthScope Consortium were used for access to waveforms and related metadata. These services are funded through the National Science Foundation’s Seismological Facility for the Advancement of Geoscience (SAGE) Award under Cooperative Agreement EAR-1724509. Additional computational support was provided by the Institute for Cyber-Enabled Research (ICER) at Michigan State University.

References

- Abers, G., S. Schwartz, A. Sheehan, D. Wiens, and J. Freymueller (2021). RAPID: Response to the 29 July 2021 Chignik earthquake [SEED data], International Federation of Digital Seismograph Networks, doi: [10.7914/SN/6J_2021](https://doi.org/10.7914/SN/6J_2021).
- Abers, G., D. Wiens, S. Schwartz, A. Sheehan, D. Shillington, L. Worthington, *et al.* (2018). AACSE: Alaska Amphibious Community seismic Experiment [SEED data], International Federation of Digital Seismograph Networks, doi: [10.7914/SN/XO_2018](https://doi.org/10.7914/SN/XO_2018).
- Aki, K. (1979). Characterization of barriers on an earthquake fault, *J. Geophys. Res.* **84**, no. B11, 6140–6148, doi: [10.1029/JB084iB11p06140](https://doi.org/10.1029/JB084iB11p06140).
- Alaska Earthquake Center, University of Alaska Fairbanks (1987). Alaska Geophysical Network [SEED data], *International Federation of Digital Seismograph Networks*, doi: [10.7914/SN/AK](https://doi.org/10.7914/SN/AK).
- Alaska Volcano Observatory/U.S. Geological Survey (USGS) (1988). Alaska Volcano Observatory [SEED data], *International Federation of Digital Seismograph Networks*, doi: [10.7914/SN/AV](https://doi.org/10.7914/SN/AV).
- Bai, Y., C. Liu, T. Lay, K. F. Cheung, and Y. Yamazaki (2023). Fast and slow intraplate ruptures during the 19 October 2020 magnitude 7.6 Shumagin earthquake, *Nat. Commun.* **14**, no. 1, 2015, doi: [10.1038/s41467-023-37731-2](https://doi.org/10.1038/s41467-023-37731-2).
- Bécel, A., D. J. Shillington, M. Delescluse, M. R. Nedimović, G. A. Abers, D. M. Saffer, *et al.* (2017). Tsunamigenic structures in a creeping section of the Alaska subduction zone, *Nature Geosci.* **10**, no. 8, 609–613, doi: [10.1038/ngeo2990](https://doi.org/10.1038/ngeo2990).
- Ben-Zion, Y., and J. R. Rice (1995). Slip patterns and earthquake populations along different classes of faults in elastic solids, *J. Geophys. Res.* **100**, no. B7, 12,959–12,983, doi: [10.1029/94JB03037](https://doi.org/10.1029/94JB03037).
- Beyreuther, M., R. Barsch, L. Krischer, T. Megies, Y. Behr, and J. Wassermann (2010). ObsPy: A Python toolbox for seismology, *Seismol. Res. Lett.* **81**, no. 3, 530–533, doi: [10.1785/gssrl.81.3.530](https://doi.org/10.1785/gssrl.81.3.530).
- Bondár, I., and D. Storchak (2011). Improved location procedures at the International Seismological Centre, *Geophys. J. Int.* **186**, no. 3, 1220–1244, doi: [10.1111/j.1365-246X.2011.05107.x](https://doi.org/10.1111/j.1365-246X.2011.05107.x).
- Brunns, T. R., R. von Huene, S. D. Lewis, and J. W. Ladd (1987). Geology and Petroleum Potential of the Shumagin Margin, Alaska, available at https://archives.datapages.com/data/circ_pac/0007/0157_f.htm (last accessed January 2025).
- Clarke, J., D. J. Shillington, C. Regalla, J. B. Gaherty, J. Estep, D. A. Wiens, *et al.* (2024). Controls on bending-related faulting offshore of the Alaska Peninsula, *Geochem. Geophys. Geosyst.* **25**, no. 3, e2023GC011271, doi: [10.1029/2023GC011271](https://doi.org/10.1029/2023GC011271).
- Contreras-Reyes, E., J. Jara, I. Grevenmeyer, S. Ruiz, and D. Carrizo (2012). Abrupt change in the dip of the subducting plate beneath north Chile, *Nature Geosci.* **5**, no. 5, 342–345, doi: [10.1038/ngeo1447](https://doi.org/10.1038/ngeo1447).
- Cowell, B. W., and D. Melgar (2020). Slipping the Shumagin gap: A kinematic coseismic and early afterslip model of the M_w 7.8 Simeonof Island, Alaska, earthquake, *Geophys. Res. Lett.* **47**, no. 19, e2020GL090308, doi: [10.1029/2020GL090308](https://doi.org/10.1029/2020GL090308).
- Davies, J., L. Sykes, L. House, and K. Jacob (1981). Shumagin seismic gap, Alaska Peninsula: History of great earthquakes, tectonic setting, and evidence for high seismic potential, *J. Geophys. Res.* **86**, no. B5, 3821–3855, doi: [10.1029/JB086iB05p03821](https://doi.org/10.1029/JB086iB05p03821).
- Drooff, C., and J. T. Freymueller (2021). New constraints on slip deficit on the Aleutian megathrust and inflation at Mt. Veniaminof, Alaska from repeat GPS measurements, *Geophys. Res. Lett.* **48**, no. 4, e2020GL091787, doi: [10.1029/2020GL091787](https://doi.org/10.1029/2020GL091787).
- Dziewonski, A. M., T.-A. Chou, and J. H. Woodhouse (1981). Determination of earthquake source parameters from waveform data for studies of global and regional seismicity, *J. Geophys. Res.* **86**, no. B4, 2825–2852, doi: [10.1029/JB086iB04p02825](https://doi.org/10.1029/JB086iB04p02825).
- Ekström, G., M. Nettles, and A. M. Dziewoński (2012). The global CMT project 2004–2010: Centroid-moment tensors for 13,017 earthquakes, *Phys. Earth Planet. Int.* **200–201**, 1–9, doi: [10.1016/j.pepi.2012.04.002](https://doi.org/10.1016/j.pepi.2012.04.002).
- Elliott, J. L., R. Grapenthin, R. M. Parameswaran, Z. Xiao, J. T. Freymueller, and L. Fusso (2022). Cascading rupture of a mega-thrust, *Sci. Adv.* **8**, no. 18, eabm4131, doi: [10.1126/sciadv.abm4131](https://doi.org/10.1126/sciadv.abm4131).

- Faccenda, M. (2014). Water in the slab: A trilogy, *Tectonophysics* **614**, 1–30, doi: [10.1016/j.tecto.2013.12.020](https://doi.org/10.1016/j.tecto.2013.12.020).
- Freymueller, J. T., E. N. Suleimani, and D. J. Nicolsky (2021). Constraints on the slip distribution of the 1938 M_W 8.3 Alaska Peninsula earthquake from tsunami modeling, *Geophys. Res. Lett.* **48**, no. 9, e2021GL092812, doi: [10.1029/2021GL092812](https://doi.org/10.1029/2021GL092812).
- USGS (2016). U.S. Geological Survey Networks [SEED data], *International Federation of Digital Seismograph Networks*, doi: [10.7914/SN/GM](https://doi.org/10.7914/SN/GM).
- Hayes, G. P., G. L. Moore, D. E. Portner, M. Hearne, H. Flamme, M. Furtney, and G. M. Smoczyk (2018). Slab2, a comprehensive subduction zone geometry model, *Science* **362**, no. 6410, 58–61, doi: [10.1126/science.aat4723](https://doi.org/10.1126/science.aat4723).
- Herman, M. W., and K. P. Furlong (2021). Triggering an unexpected earthquake in an uncoupled subduction zone, *Sci. Adv.* **7**, no. 13, doi: [10.1126/sciadv.abf7590](https://doi.org/10.1126/sciadv.abf7590).
- Hicks, S. P., and A. Rietbrock (2015). Seismic slip on an upper-plate normal fault during a large subduction megathrust rupture, *Nature Geosci.* **8**, no. 12, 955–960, doi: [10.1038/ngeo2585](https://doi.org/10.1038/ngeo2585).
- Horowitz, W. L., P. J. Hoose, D. A. Steffy, and R. F. Turner (1989). *Geologic Report for the Shumagin Planning Area, Western Gulf of Alaska*, U.S. Department of the Interior, Minerals Management Service, Alaska OCS Region.
- Hu, J., and M. Gurnis (2020). Subduction duration and slab dip, *Geochem. Geophys. Geosyst.* **21**, no. 4, e2019GC008862, doi: [10.1029/2019GC008862](https://doi.org/10.1029/2019GC008862).
- Incorporated Research Institutions for Seismology (IRIS) Transportable Array (2003). USArray Transportable Array [SEED data], *International Federation of Digital Seismograph Networks*, doi: [10.7914/SN/TA](https://doi.org/10.7914/SN/TA).
- International Seismological Centre (ISC) Bulletin (2018). [Data set], International Seismological Centre, doi: [10.31905/D808B830](https://doi.org/10.31905/D808B830).
- Jiang, Y., P. J. González, and R. Bürgmann (2022). Subduction earthquakes controlled by incoming plate geometry: The 2020 $M > 7.5$ Shumagin, Alaska, earthquake doublet, *Earth Planet. Sci. Lett.* **584**, 117,447, doi: [10.1016/j.epsl.2022.117447](https://doi.org/10.1016/j.epsl.2022.117447).
- Kuehn, H., M. R. Nedimović, D. J. Shillington, and A. Bécel (2024). Variations in reflection signature and slip behavior. Tectonics and seismic structure of Alaska and Northwestern Canada, *EarthScope and Beyond*, 419.
- Li, J., D. J. Shillington, A. Bécel, M. R. Nedimović, S. C. Webb, D. M. Saffer, et al. (2015). Downdip variations in seismic reflection character: Implications for fault structure and seismogenic behavior in the Alaska subduction zone, *J. Geophys. Res.* **120**, no. 11, 7883–7904, doi: [10.1002/2015JB012338](https://doi.org/10.1002/2015JB012338).
- Li, Z., D. A. Wiens, W. Shen, and D. J. Shillington (2024). Along-strike variations of Alaska subduction zone structure and hydration determined from amphibious seismic data, *J. Geophys. Res.* **129**, no. 3, e2023JB027800, doi: [10.1029/2023JB027800](https://doi.org/10.1029/2023JB027800).
- Liu, C., Y. Bai, T. Lay, Y. Feng, and X. Xiong (2023). Megathrust complexity and the up-dip extent of slip during the 2021 Chignik, Alaska Peninsula earthquake, *Tectonophysics* **854**, 229,808, doi: [10.1016/j.tecto.2023.229808](https://doi.org/10.1016/j.tecto.2023.229808).
- Liu, C., T. Lay, and X. Xiong (2022). The 29 July 2021 M_W 8.2 Chignik, Alaska Peninsula earthquake rupture inferred from seismic and geodetic observations: Re-rupture of the western 2/3 of the 1938 rupture zone, *Geophys. Res. Lett.* **49**, no. 4, e2021GL096004, doi: [10.1029/2021GL096004](https://doi.org/10.1029/2021GL096004).
- Mousavi, S. M., and G. C. Beroza (2022). Deep-learning seismology, *Science* **377**, no. 6607, eabm4470, doi: [10.1126/science.abm4470](https://doi.org/10.1126/science.abm4470).
- Mousavi, S. M., W. L. Ellsworth, W. Zhu, L. Y. Chuang, and G. C. Beroza (2020). Earthquake transformer—An attentive deep-learning model for simultaneous earthquake detection and phase picking, *Nat. Commun.* **11**, no. 1, 3952, doi: [10.1038/s41467-020-17591-w](https://doi.org/10.1038/s41467-020-17591-w).
- National Oceanic and Atmospheric Administration (NOAA). (1967). National Tsunami Warning Center Alaska Seismic Network [SEED data], *International Federation of Digital Seismograph Networks*, doi: [10.7914/SN/AT](https://doi.org/10.7914/SN/AT).
- Park, Y., S. M. Mousavi, W. Zhu, W. L. Ellsworth, and G. C. Beroza (2020). Machine-learning-based analysis of the Guy-Greenbrier, Arkansas earthquakes: A tale of two sequences, *Geophys. Res. Lett.* **47**, no. 6, e2020GL087032, doi: [10.1029/2020GL087032](https://doi.org/10.1029/2020GL087032).
- Ruppert, N. A., G. Barchek, and G. A. Abers (2022). Enhanced regional earthquake catalog with Alaska amphibious community seismic experiment data, *Seismol. Res. Lett.* doi: [10.1785/0220220226](https://doi.org/10.1785/0220220226).
- Scripps Institution of Oceanography (1986). Global Seismograph Network - IRIS/IDA [SEED data], *International Federation of Digital Seismograph Networks*, doi: [10.7914/SN/II](https://doi.org/10.7914/SN/II).
- Segall, P., and D. D. Pollard (1980). Mechanics of discontinuous faults, *J. Geophys. Res.* **85**, no. B8, 4337–4350, doi: [10.1029/JB085iB08p04337](https://doi.org/10.1029/JB085iB08p04337).
- Senapati, B., E. O. Lindsey, B. Kundu, D. Panda, D. K. Tiwari, and R. K. Yadav (2024). ‘Double Puzzle’ at the Shumagin seismic gap, Alaska Peninsula: Intralab strike-slip faulting loaded by lateral variations in megathrust fault friction, *Geophys. J. Int.* **236**, no. 3, 1471–1483, doi: [10.1093/gji/gjaa002](https://doi.org/10.1093/gji/gjaa002).
- Shillington, D. J., A. Bécel, and M. R. Nedimović (2022). Upper plate structure and megathrust properties in the Shumagin gap near the July 2020 $M 7.8$ Simeonof event, *Geophys. Res. Lett.* **49**, no. 2, e2021GL096974, doi: [10.1029/2021GL096974](https://doi.org/10.1029/2021GL096974).
- Shillington, D. J., A. Bécel, M. R. Nedimović, H. Kuehn, S. C. Webb, G. A. Abers, et al. (2015). Link between plate fabric, hydration and subduction zone seismicity in Alaska, *Nature Geosci.* **8**, no. 12, 961–964, doi: [10.1038/ngeo2586](https://doi.org/10.1038/ngeo2586).
- Tan, Y. J., F. Waldhauser, W. L. Ellsworth, M. Zhang, W. Zhu, M. Michele, et al. (2021). Machine-learning-based high-resolution earthquake catalog reveals how complex fault structures were activated during the 2016–2017 central Italy sequence, *Seism. Rec.* **1**, no. 1, 11–19, doi: [10.1785/0320210001](https://doi.org/10.1785/0320210001).
- Tape, C., and A. Lomax (2022). Aftershock regions of Aleutian-Alaska megathrust earthquakes, 1938–2021, *J. Geophys. Res.* **127**, no. 7, e2022JB024336, doi: [10.1029/2022JB024336](https://doi.org/10.1029/2022JB024336).
- von Huene, R., J. J. Miller, and A. Krabbendhoef (2021). The Alaska convergent margin Backstop Splay fault zone, a potential large tsunami generator between the frontal prism and continental framework, *Geochem. Geophys. Geosyst.* **22**, no. 1, e2019GC008901, doi: [10.1029/2019GC008901](https://doi.org/10.1029/2019GC008901).
- Wang, F., S. S. Wei, C. Drooff, J. L. Elliott, J. T. Freymueller, N. A. Ruppert, and H. Zhang (2024). Fluids control along-strike variations in the Alaska megathrust slip, *Earth Planet. Sci. Lett.* **633**, 118,655, doi: [10.1016/j.epsl.2024.118655](https://doi.org/10.1016/j.epsl.2024.118655).

- Wang, F., S. S. Wei, N. A. Ruppert, H. Zhang, and J. Wu (2025). Slab morphology, dehydration, and sub-arc melting beneath the Alaska Peninsula revealed by body-wave tomography, *J. Geophys. Res.* **130**, no. 3, e2024JB029814, doi: [10.1029/2024JB029814](https://doi.org/10.1029/2024JB029814).
- Wei, S. S., P. Ruprecht, S. L. Gable, E. G. Huggins, N. Ruppert, L. Gao, and H. Zhang (2021). Along-strike variations in intermediate-depth seismicity and arc magmatism along the Alaska Peninsula, *Earth Planet. Sci. Lett.* **563**, 116,878, doi: [10.1016/j.epsl.2021.116878](https://doi.org/10.1016/j.epsl.2021.116878).
- Wetzler, N., T. Lay, E. E. Brodsky, and H. Kanamori (2018). Systematic deficiency of aftershocks in areas of high coseismic slip for large subduction zone earthquakes, *Sci. Adv.* **4**, no. 2, eaao3225, doi: [10.1126/sciadv.aao3225](https://doi.org/10.1126/sciadv.aao3225).
- Xi, Z., S. S. Wei, W. Zhu, G. C. Beroza, Y. Jie, and N. Saloor (2024). Deep learning for deep earthquakes: Insights from OBS observations of the Tonga subduction zone, *Geophys. J. Int.* **238**, no. 2, 1073–1088, doi: [10.1093/gji/ggae200](https://doi.org/10.1093/gji/ggae200).
- Xiao, Z., J. T. Freymueller, R. Grapenthin, J. L. Elliott, C. Drooff, and L. Fusso (2021). The deep Shumagin gap filled: Kinematic rupture model and slip budget analysis of the 2020 M_w 7.8 Simeonof earthquake constrained by GNSS, global seismic waveforms, and floating InSAR, *Earth Planet. Sci. Lett.* **576**, 117,241, doi: [10.1016/j.epsl.2021.117241](https://doi.org/10.1016/j.epsl.2021.117241).
- Yang, L., J. Wang, and C. Xu (2023). Coseismic Coulomb stress changes induced by the 2020–2021 Alaska earthquake sequence in and around the Shumagin gap and their influence on the Alaska-Aleutian subduction interface, *Geod. Geodyn.* doi: [10.1016/j.geog.2023.04.007](https://doi.org/10.1016/j.geog.2023.04.007).
- Ye, L., Y. Bai, D. Si, T. Lay, K. F. Cheung, and H. Kanamori (2022). Rupture model for the 29 July 2021 M_w 8.2 Chignik, Alaska earthquake constrained by seismic, geodetic, and tsunami observations, *J. Geophys. Res.* **127**, no. 7, e2021JB023676, doi: [10.1029/2021JB023676](https://doi.org/10.1029/2021JB023676).
- Ye, L., T. Lay, H. Kanamori, Y. Yamazaki, and K. F. Cheung (2021). The 22 July 2020 M 7.8 Shumagin seismic gap earthquake: Partial rupture of a weakly coupled megathrust, *Earth Planet. Sci. Lett.* **562**, 116,879, doi: [10.1016/j.epsl.2021.116879](https://doi.org/10.1016/j.epsl.2021.116879).
- Zhang, H., and C. H. Thurber (2003). Double-difference tomography: The method and its application to the Hayward fault, California, *Bull. Seismol. Soc. Am.* **93**, no. 5, 1875–1889, doi: [10.1785/0120020190](https://doi.org/10.1785/0120020190).
- Zhang, Y., R. Wang, T. R. Walter, W. Feng, Y. Chen, and Q. Huang (2017). Significant lateral dip changes may have limited the scale of the 2015 M_w 7.8 Gorkha earthquake, *Geophys. Res. Lett.* **44**, no. 17, 8847–8856, doi: [10.1002/2017GL074095](https://doi.org/10.1002/2017GL074095).
- Zhu, W., and G. C. Beroza (2019). PhaseNet: A deep-neural-network-based seismic arrival-time picking method, *Geophys. J. Int.* **216**, no. 1, 261–273, doi: [10.1093/gji/ggy423](https://doi.org/10.1093/gji/ggy423).
- Zhu, W., I. W. McBrearty, S. M. Mousavi, W. L. Ellsworth, and G. C. Beroza (2022). Earthquake phase association using a Bayesian Gaussian mixture model, *J. Geophys. Res.* **127**, no. 5, e2021JB023249, doi: [10.1029/2021JB023249](https://doi.org/10.1029/2021JB023249).
- Zhu, W., B. Rong, Y. Jie, and S. S. Wei (2025). Robust earthquake location using random sample consensus (RANSAC), arXiv, doi: [10.48550/arXiv.2502.10933](https://doi.org/10.48550/arXiv.2502.10933).

Manuscript received 26 February 2025

Published online 10 September 2025